

Planet Migration through a Self-Gravitating Planetesimal Disk

Alex Moore, Alice C. Quillen, & Richard G. Edgar

Department of Physics and Astronomy, University of Rochester, Rochester, NY 14627, USA

11 June 2021

ABSTRACT

We simulate planet migration caused by interactions between planets and a planetesimal disk. We use an N-body integrator optimized for near-Keplerian motion that runs in parallel on a video graphics card, and that computes all pair-wise gravitational interactions. We find that the fraction of planetesimals found in mean motion resonances is reduced and planetary migration rates are on average about 50% slower when gravitational interactions between the planetesimals are computed than when planetesimal self-gravity is neglected. This is likely due to gravitational stirring of the planetesimal disk that is not present when self-gravity is neglected that reduces their capture efficiency because of the increased particle eccentricity dispersion. We find that migration is more stochastic when the disk is self-gravitating or comprised of more massive bodies. Previous studies have found that if the planetesimal disk density is below a critical level, migration is “damped” and the migration rate decays exponentially, otherwise it is “forced” and the planet’s migration rate could accelerate exponentially. Migration rates measured from our undamped simulations suggest that the migration rate saturates at a level proportional to disk density and subsequently is approximately power law in form with time.

1 INTRODUCTION

The field of solar system dynamics, has a timeline of discoveries that is related to the computational power available (e.g., Morbidelli 2001). As computational power has increased over time, so to has our ability to more accurately simulate more complex systems. The interaction between planets and planetesimals subsequent to formation is a well posed n-body problem but displays remarkable complexity even in the absence of collisions, including resonance capture, planetary migration, and heating and scattering of planetesimals. In this paper we attempt to more accurately simulate this system by using the increased computational power and on board memory recently available on video graphics cards.

Planet-planetesimal scattering can lead to planet migration (e.g., Fernandez & Ip 1984; Malhotra 1995; Hahn & Malhotra 1999; Ida et al. 2000; Levison & Morbidelli 2003; Gomes et al. 2004, 2005; Hahn & Malhotra 2005; Levison et al. 2008). Recent work on dusty circumstellar disks with clearings, suggest that planets are required to account for the morphology of the disk (Quillen 2006a; Wyatt 2006). The planetesimal masses suggested by collisional models (e.g., Wyatt & Dent 2002; Dominik & Decin 2003; Quillen et al. 2007) and proximity of the hypothetical planet to the disks for systems such as Fomalhaut intimate that planetary migration could be taking place. To simulate planet migration due to planetesimal scattering, planets must gravitationally interact with

planetesimals. However, because of the $O(N^2)$ required computational intensity previous simulations have necessarily neglected the gravitational interactions between the planetesimals (e.g., Hahn & Malhotra 1999; Gomes et al. 2004; Hahn & Malhotra 2005; Thommes et al. 2008). This means that collective gravitational effects and gravitational self stirring in the disk have been ignored. Here we take all interparticle forces into account to explore what differences might be seen in simulations of migrating planets with and without planetesimal interactions.

2 NUMERICAL SIMULATIONS

The migration simulations were carried out using an N-body code running on a 4 node cluster running the “Mars Hill” Rocks 4.3 Linux operating system (a CentOS based distribution) that hosts 4 NVIDIA GeForce 8800 GTX graphics cards. The code was run on the graphics processing units (GPUs) residing on the graphics cards and is written with NVIDIA’s CUDA (Compute Unified Device Architecture), a C-language development environment for CUDA enabled GPUs. CUDA is a GPGPU (General-purpose computing on graphics processing units) technology that allows a programmer to use the C programming language to code algorithms for execution on the graphics processing unit. Its intention is to expose the hardware to the developer through a memory management model that encourages both constant streaming of data as well as massive parallelization.

2.1 A second order democratic heliocentric method symplectic integrator for the GPU

We have modified the second order symplectic integrator introduced by (Duncan et al. 1998), also known as the democratic heliocentric method, so that it runs on a GPU. We have chosen the democratic heliocentric method because the force from the central body is separated from the integration of the remainder of the particles and the coordinates do not depend on the order of the particles. This increases the accuracy of the integrator when there are large mass differences and is particularly desirable when forced to work in floating point single precision. When we obtain video cards that can compute in double precision the code will improve in precision. The move to double precision will also allow us to extend the range of the planetesimal masses simulated.

In heliocentric coordinates and barycentric momenta (Wisdom, Holman & Touma 1996) the Hamiltonian of the system can be written

$$H = H_{Sun} + H_{Kep} + H_{Int} \quad (1)$$

where

$$H_{Sun} = \frac{1}{2m_0} \left| \sum_{i=1}^n \mathbf{P}_i^2 \right|^2 \quad (2)$$

is a linear drift term and P_i are the barycentric momenta. Here m_0 is the central particle mass. The second term H_{Kep} is the sum of Keplerian Hamiltonians for all particles with respect to the central body,

$$H_{Kep} = \sum_{i=0}^N \left(\frac{\mathbf{P}_i^2}{2m_i} - \frac{Gm_i m_0}{|\mathbf{Q}_i|} \right) \quad (3)$$

where \mathbf{Q}_i are the heliocentric coordinates and are conjugate to the barycentric momenta. Here m_i is the mass of the i -th particle and G is the gravitational constant. The interaction term contains all gravitational interaction terms except those to the central body,

$$H_{Int} = \sum_{i=1}^N \sum_{j=1, j \neq i}^N -\frac{Gm_i m_j}{2|\mathbf{Q}_i - \mathbf{Q}_j|}. \quad (4)$$

The second order single timestep integrator advances with timestep τ using evolution operators (e.g., Yoshida 1990)

$$E_{Sun} \left(\frac{\tau}{2} \right) E_{Kep} \left(\frac{\tau}{2} \right) E_{Int}(\tau) E_{Kep} \left(\frac{\tau}{2} \right) E_{Sun} \left(\frac{\tau}{2} \right) \quad (5)$$

where we have reversed the order of the Keplerian evolution and the interaction steps compared to that discussed by (Duncan et al. 1998). We have done this to reduce the total number of computations per timestep. The Keplerian advance requires $O(N)$ computations but interaction term requires $O(N^2)$ computations.

The drift evolution operator requires computation of the sum of the momenta. We have implemented this using a parallel reduction sum algorithm available with the NVIDIA CUDA Software Development Kit (SDK) 1.1 that is similar to the scan prefix sum algorithm (Harris et al. 2008).

The Keplerian step was implemented with f and g functions using the universal differential Kepler's equation (Prussing & Conway 1993) so that bound and unbound particles can both be integrated with the same routine. The

Keplerian evolution step is also done on the GPU with each thread computing the evolution for a separate particle. The dominant source of error is in the Keplerian evolution step and is due to the single floating point precision. These errors can cause a systematic radial drift that does not average to zero. To minimize errors caused by the single precision computation during the Kepler advances we chose f and g functions that maintain angular momentum conservation across each evolution step. The positions and velocities at a later time can be written in terms of those at an earlier time

$$\begin{aligned} \vec{\mathbf{x}}_1 &= f\vec{\mathbf{x}}_0 + g\vec{\mathbf{v}}_0 \\ \vec{\mathbf{v}}_1 &= \dot{f}\vec{\mathbf{x}}_0 + \dot{g}\vec{\mathbf{v}}_0. \end{aligned} \quad (6)$$

The angular momentum at the later time, $\vec{\mathbf{L}}_1$ can be written in terms of that at the earlier time, $\vec{\mathbf{L}}_0$,

$$\vec{\mathbf{L}}_1 = (f\dot{g} - g\dot{f})(\vec{\mathbf{x}}_0 \times \vec{\mathbf{v}}_0) = (f\dot{g} - g\dot{f})\vec{\mathbf{L}}_0. \quad (7)$$

Conservation of angular momentum yields the condition

$$f\dot{g} - g\dot{f} = 1. \quad (8)$$

We utilize this formula to solve for one of the 4 functions reducing the inward radial drift resulting by the single precision computation during the Keplerian advances.

The interaction terms are computed on the GPU with all N^2 force pairs evaluated explicitly in parallel. The algorithm is based on the algorithm described by (Nyland, Harris, & Prins 2008). This algorithm takes advantage of fast shared memory on board the GPU to simultaneously compute all forces in a $p \times p$ tile of particle positions, where p is the number of threads chosen for the computation (typically 256). The total energy was evaluated with a kernel explicitly evaluating all N^2 pair potential energy terms, similar to that calculating all N^2 forces.

After the change to heliocentric/barycentric coordinates, the position of the first coordinate corresponds to the center of mass and center of momentum. The trajectory of this particle need not be integrated. However it is convenient to calculate the energy using all pair interactions including the central mass. The interaction term in the Keplerian part of the Hamiltonian can be computed at the same times as H_{Int} if \mathbf{Q}_0 is set to zero. Consequently we set $\mathbf{Q}_0 = \mathbf{P}_0 = 0$ at the beginning of the computation. This is equivalent to working in the center of mass and momentum reference frame. Because we would like to be able to quickly check the total energy, we have chosen to keep the first particle corresponding to the center of mass and momentum as the first element in the position and velocity arrays. During computation of H_{Int} we set m_0 to zero so that force terms from the first particle are not computed. These are already taken into account in the evolution term corresponding to H_{Kep} . The mass is restored during the energy sum computation as all potential energy terms must be calculated explicitly.

The location of memory should be considered when running routines as data transfer between the CPU and GPU can slow the code. The maximum theoretical throughput of PCI-express 16x bus technology, the interlink between the CPU and GPU on Intel processor based motherboards, is 4 GB/s with a significantly higher latency than on device memory transfers. Depending on GPU design, theoretical memory transfer throughputs can approach 100 GB/s, as is

the case for the 8800 GTX which has a theoretical throughput of 86.4 GB/s. Reducing the number of data transfers between the CPU and GPU not only reduces the CPU clock time required for a calculation, but also reduces the number of calls which have higher latency. CPU and GPU global memory access is a significant bottleneck compared to the actual number of clock cycles required for a specific calculation with the former containing a much higher performance penalty due to latency. For this reason, positions and velocities for all particles are kept in global memory on board the GPU device. Arrays for both current and previous time step positions are required during the interaction step computation. The particle positions and velocities are only transferred back into host or CPU accessible memory to output data files. An additional float vector of length equal to the number of particles is allocated in global memory on the device to compute the momentum sums used in the drift step computation. Shared memory on the GPU is used during the all pairs interaction computation step and during the reduction sum. Shared memory on the GPU drastically increases the speed of calculations because the use of shared memory has almost no latency penalty compared to that of both the CPU and the GPU global memory. By streaming information from global memory to shared memory, we are able to hide the latency of global memory, further increasing the computation speed. Though the maximum number of threads on the video card we used is 512, we found that register space on the GPU limited the interaction step computation to 256 threads per block due to its complexity. A more detailed review of NVIDIA GPU hardware and programming techniques can be found in the CUDA Programming Guide.

We work in a lengthscale in units of the outermost planet’s initial semi-major axis and with a timescale such that $GM_* = 1$ where M_* is the mass of the central star.

2.2 Code Checks

The following self-consistency checks on the code were performed. We checked that two body dynamics is preserved for all particles when all masses but the central one are zero. In this case the orbital elements (excepting the mean anomaly) are conserved at the level of the precision of computation. We checked that the energy computation computed in heliocentric/barycentric coordinates is consistent with that computed in Cartesian coordinates. We checked that the conversion to heliocentric/barycentric coordinates followed by inverse conversion returns the initial coordinates. We checked that the force and potential energy terms computed on the GPU are consistent with those computed on CPU. We checked that the N-body simulation without Keplerian integration conserves energy. We note that the order of some of the arguments in the SDK1.1 nbody kernel were inconsistent with the correct order described by (Nyland, Harris, & Prins 2008). To conserve energy we corrected the order of the arguments in the force computation step from that in the SDK1.1 nbody kernel. We checked that integrating a two body system conserves energy. We ran a test case identical to that run by Bromley & Kenyon (2006) and shown in their Figure 5 with similar results (though see discussion on energy conservation in the next section). This corresponds to 2 earth mass planets embedded in a uniform

disk of 800 objects 1/100 of the mass of the planets. This test case was also integrated by Kokubo & Ida (1995).

2.3 Simulation Checks

The second set of checks was done by running full simulations in order to determine the smoothing length and time step requirements and restrictions. In one test we varied the time step significantly in order to measure the impact of larger time steps on our accuracy. A larger timestep would allow us to run the simulation for more orbital periods. We ran full 10^4 particle simulations over thousands of orbits and noted that varying the time step resulted in little difference in the total energy measured. In our second test, we varied the softening length in 2 different sets of simulations. At extremely small softening length values we note that the simulated system becomes extremely stochastic. The reverse effect is exhibited when we make the smoothing length extremely large. This effect was previously noted in (Kokubo & Ida 1995) and happens because our simulation does not adjust the time step to take into account collisions and close encounters. Since the simulation steps are small enough to allow "smooth" or nearly continuous updates, there is the possibility that a close encounter between two objects will be forced by the step which may have never occurred physically. If the softening length is made too large, the forces between objects that are having close encounters is reduced unrealistically. The softening length is chosen to help prevent this from happening. Kokubo & Ida (1995) selects a softening parameter set as

$$R_{min} = \frac{r_H}{200} \quad (9)$$

where r_H is the Hill radius of a planetesimal. This leads to a Hill radius which is roughly equivalent to the physical radius of a protoplanet at 1AU. Given these parameters, we chose a variety of smoothing lengths that were on the same order of magnitude and did not note a significant any significant deviations between the results of the simulations. The smoothing length and timestep were not adjusted during the simulation.

2.4 Benchmarks

We measured the time to run our code on on the NVIDIA GeForce 8800 GTX graphics cards. The timing included the delay to send the job out to the individual nodes of the cluster, initial disk generation and input and output of files. We ran a simulation of a disk with 2 planets, one at semi-major axis $a = 1$ with the other interior to this. The planet masses were 10^{-3} of that of the star. The planets were surrounded by a disk of particles with mass 10^{-7} of that of the central star. Time units were set such that $GM_* = 1$. The time step was 0.1 or $0.1/(2\pi) = 0.0159$ of the outer planet’s orbit. For 10^4 particles 1000 timesteps ran with 0.137 s per timestep. For 10^5 particles 100 timesteps ran with 57s per timestep and similar error. The energy fraction error was 10^{-3} throughout the entire simulation and drifts downward systematically with time such that the system becomes increasingly bound. The systematic loss of energy and associated radial inward drift we have determined is caused by the

single point floating precision for calculations done during the Kepler advances.

2.5 Initial conditions

In this paper we primarily discuss simulations with 2 planets and an exterior annulus of planetesimals. The initial planetesimal disk has a flat distribution in semi-major axis so that the surface density is proportional to $1/r$ for radius r . An isotropic disk is generated with initial eccentricity and inclination dispersion such that $\langle e^2 \rangle = 2\langle i^2 \rangle$ and initial inclination dispersion set to 0.01. The smoothing length was typically set to be slightly smaller than the mean interparticle spacing. Typical mean spacing values for 10^4 particles in units of the inner planet's semi-major axis was around 0.01, with our smoothing length set correspondingly to 0.01. The smoothing length spacing was set the same for all simulations. The timestep was set at 0.1 where the orbital period of the inner planet is 2π . A timestep of 0.1 is convenient because it ensures accuracy while still allowing of order 10^3 orbital periods to be completed within 24 hours for 10^4 particles. Comparisons between simulations with timesteps of 0.2, 0.1 and 0.05 yielded only insignificant differences in planetary migration rates, indicating that our simulations are not strongly sensitive to the chosen time step. All other parameters are listed in table 1. The initial semi-major axes of the planetesimals ranges from 1.5 to 3.0. We work in units of the outermost planet's initial semi-major axis and with $GM_* = 1$ so that the initial period of the outermost planet is 2π . We discuss most timescales in units of the outermost planet's initial rotation period. The initial inclination and eccentricity of the two planets were set to zero. However, we have found that planet eccentricities and inclinations rapidly settled toward zero for the planetesimal disks considered here. All simulations were run for approximately 4000 orbits.

2.6 Comparison code lacking forces between planetesimals

Our code can compute all interparticle forces, however most planet migration simulations have neglected forces between planetesimals. We desire a direct comparison between simulations that take into account all inter particles forces and those that neglect forces between planetesimals. To do this we run two versions of our code that are identical except that interparticle forces are not computed if both particle masses are below that of a planet. In all other respects the two sets of simulations are identical.

3 MIGRATION OF 2 PLANET SYSTEMS

We begin our study of migration with the simplest system that allows migration of the outer planet into the disk; that of two planets just inside an initially cold (low velocity dispersion) annulus of planetesimals. Our first set of simulation has a inner planet with mass 10^{-3} of that of the central star (similar to Jupiter) and an outer planet with a mass ratio of 5×10^{-5} (similar to Uranus). A low mass was initially chosen for the outer planet so that outer disk is not completely disrupted during migration. A mass similar to that of

Uranus was chosen simply because in our test runs it showed the most interesting variation in its migration rate. Larger planet masses showed increasing disk disruption while lower masses showed greater degrees of stochastic motion. A high mass inner planet was initially chosen to ensure that particles can be efficiently scattered by the outer planet and subsequently ejected by the inner planet. While this mechanism can function for an inner planet that has mass ratio less than 10^{-3} , the migration of the outer planet is then more sensitive to the distance between the planets. Our choice of a large inner planet reduces the dependence on the distance between the planets. If the distance between the two planets is large then it takes longer for the outer planet to scatter particles sufficiently that they cross the inner planet's orbit.

The parameters of our simulations are listed in table 1. Three sets of simulations are run. The first ten, denoted C1-C10, include all pair-wise forces and contain a range of planetesimal disk masses and number of planetesimals. In these simulations the planetesimal mass is fixed at 10^{-7} of the stellar mass. The most massive disks simulated (simulations C1, N1, and V1-V10) have a mass ratio of 10^{-3} . This is a factor of a few larger than the more massive 200 Earth mass disks simulated by previous studies (Hahn & Malhotra 1999; Gomes et al. 2004). Simulations N1-N10 are identical to C1-C10 except forces between planetesimals are neglected. Simulations V1-V10 compute all force pairs, have the same total planetesimal disk mass, but vary the number of planetesimals and the planetesimal mass.

We first discuss the semi-major axis and eccentricity distributions during the simulations. We compare simulations with and without planetesimal self-gravity. We then discuss differences seen in the migration rates of the outer planet. Last, we consider the effects of increasing the number of particles in a simulation while maintaining a constant mass disk.

3.1 Eccentricity and semi-major axis distributions during migration

Figure 1 shows the semi-major axis vs eccentricity distribution at different times during the C1 simulation computing all force pairs for 10000 planetesimals. Each frame in the figure is separated by 200 orbital times where an orbital time corresponds to the initial orbital period of the outer planet. As can be seen from the position of the outer planet in each frame it migrates outward during the simulation. The inner planet drifts inwards but not significantly so because it is more massive than the outer planet. The particles with semi-major axis interior to the outer planet are higher after the planet has passed than they were before hand, leaving a possible signature of a migrating planet (e.g., Lufkin et al. 2006). We also notice an increase in the eccentricity dispersion of particles in the outer disk with time during the first half of the simulation.

We can compare this simulation to an identical one, denoted N1 but lacking planetesimal self-gravity. The semi-major axis and eccentricity distributions for this simulation are shown in Figure 2. The increase in eccentricity dispersion of particles in the outer disk seen in the self-gravitating disk is not present in simulation N1. Thus the eccentricity dispersion increase in the self-gravitating outer disk is

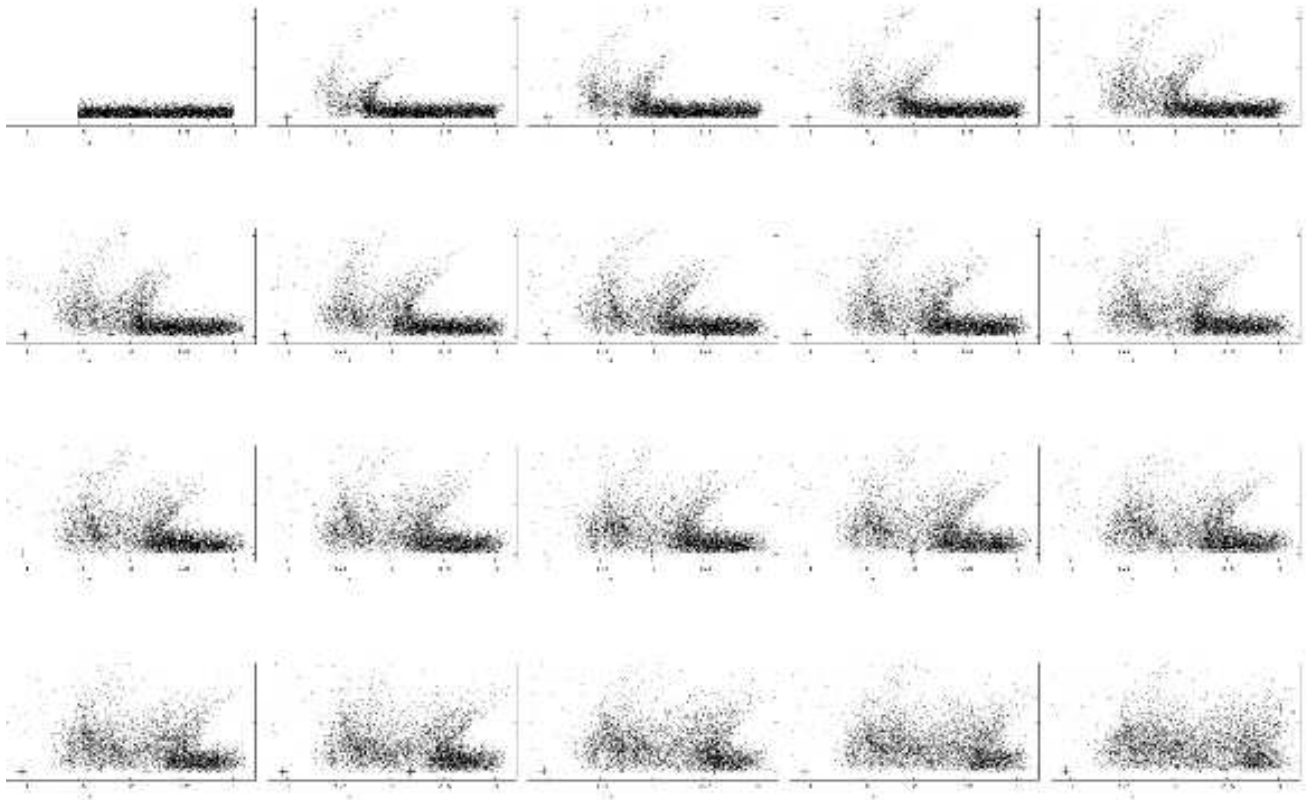


Figure 1. The semi-major axis (x -axis) vs eccentricity (y -axis) distribution of particles and planets different times during simulation C1. Each hash on the y axis is an increment of 0.2 in eccentricity starting at 0. Each hash on the x -axis is an increment of 0.5 in semi major axis, with the inner planet starting at 1.0 and the planetesimals in the disk taking an initial starting position between 1.5 and 3.0. Our migrating planet has an initial semi major axis of 1.5. This simulation has 10000 particles and computes all force pairs so that the disk feels self-gravity. Each frame is separated by 200 rotation periods based on the migrator’s initial orbital period. The two planets are shown as green crosses and the planetesimals as red dots. Two scattering surfaces are seen, one associated with each planet. These are broad features with eccentricity and semi-major axis given a particle a planet orbit crossing periastron. In the first half of the simulation the eccentricities of particles in the outer disk increases due to self-gravity. Eccentricities increase for particles that are not scattered outward as the planet passes.

likely caused by gravitational stirring of the planetesimals by themselves.

Two dominant scattering surfaces are seen as broad strokes in the semi-major axis vs eccentricity distributions of Figure 1 and 2, one each from the inner and outer planet. These surfaces correspond to particles with semi-major axis and eccentricity that have periastron crossing a planet’s orbit. Similar scattering surfaces have previously been seen in simulations of migrating planets (e.g., Gomes et al. 2004; Hahn & Malhotra 2005; Thommes et al. 2008) and imply that both planets are scattering planetesimals outwards. However, for the outer planet to migrate outwards it must also scatter planetesimals inwards. The total energy and angular momentum of material scattered outwards by the inner planet must exceed that scattered outward by the outer planet to allow it to migrate outwards. This is one of the primary reasons why we required a large inner planet mass.

When the outer planet migrates outwards it replenishes a population of moderately eccentric bodies residing between the planets. This allows the inner planet to continually scatter objects. As these objects are scattered out-

wards, they stop interacting with the outer planet allowing it to continue migrating outwards. Previous studies have described migration in terms of two regimes (e.g., Gomes et al. 2004). If the outer planet migrates at increasing slower rates, its migration is described as “damped” (e.g., Ida et al. 2000), however if it continues to migrate until it reaches the edge of the disk the migration is considered “forced” (Gomes et al. 2004). The planetesimal disks considered here are sufficiently massive that the planet migrates outwards until it is near the edge of the disk.

A comparison between Figure 1 and 2, shows little difference between the morphology of the scattering surfaces, however the location of the one associated with the outer planet is at a larger semi-major axis for simulation N1 than C1. This is because the outer planet migrates more quickly in the simulation lacking disk self-gravity (N1) than that including self-gravity (C1). We will discuss migration rates in the next subsection.

A notable difference between the simulations with and lacking disk self-gravity is the fraction of bodies captured into mean motion resonances with the outer planet. In fig-

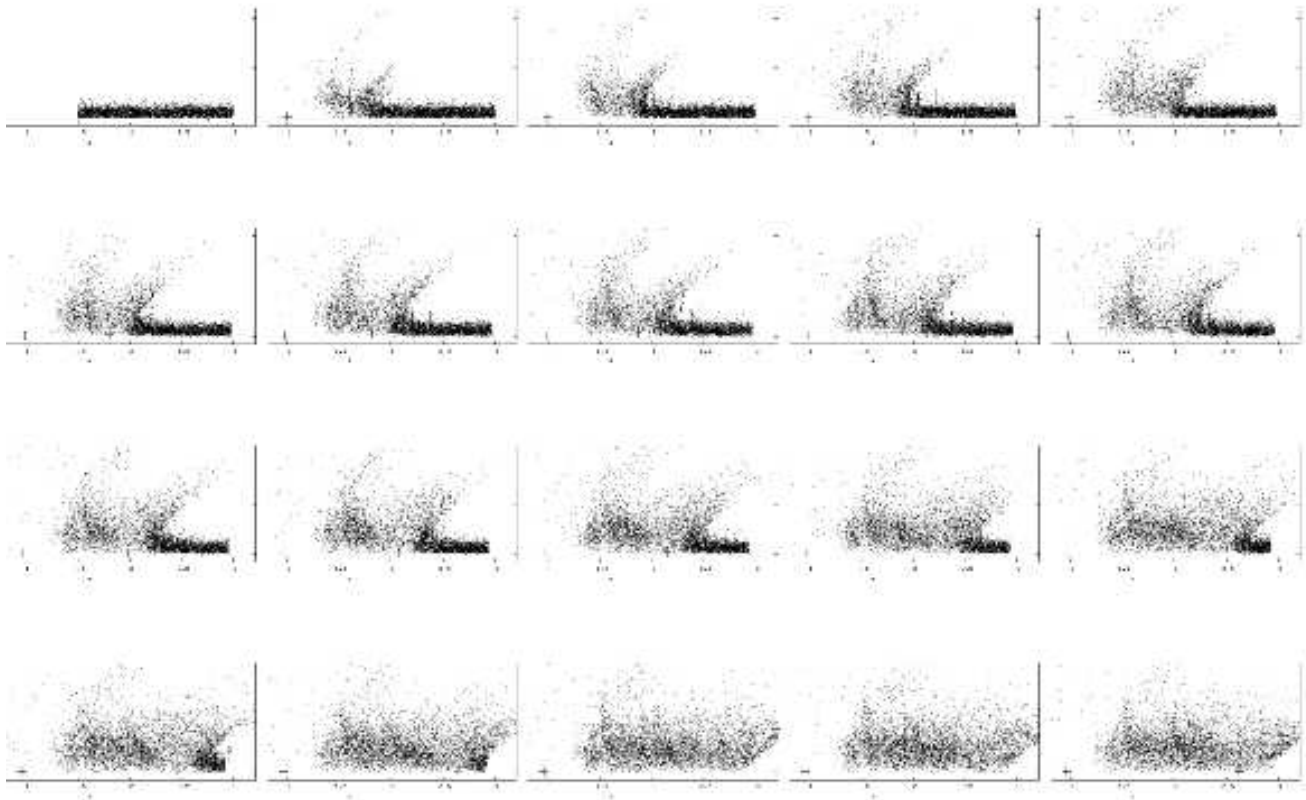


Figure 2. Similar to Figure 1 except showing the simulation N1 that is identical to C1 but lacking self-gravity in the disk. Each hash on the y axis is an increment of 0.2 in eccentricity starting at 0. Each hash on the x-axis is an increment of 0.5 in semi major axis, with the inner planet starting at 1.0 and the planetesimals in the disk taking an initial starting position between 1.5 and 3.0. Our migrating planet has an initial semi major axis of 1.5. Similar scattering surfaces are seen in this simulation. The outer planet migrates more quickly outwards than in simulation C1. The outer disk remains colder (has a lower eccentricity dispersion) during the first half of the simulation compared to the simulation with self-gravity in the disk. Populations of particles trapped in mean motion resonances with the planet are more prevalent in this simulation than in simulation C1.

ure 3 we show simulations C1 and N1 at 557 orbits into their runs (approximately 15 percent completion). We find that the fraction of particles captured into resonances is lower in the simulation with self-gravity than that without. While an outwardly migrating planet is capable of capturing bodies into mean motion resonances, the fraction of particles captured into resonance can be reduced if the planet is migrating faster or if the initial eccentricity distribution of the disk is larger (Ida et al. 2000; Hahn & Malhotra 2005; Quillen 2006b). The lifetime of particles in resonances could be reduced by scattering among the planetesimals or if the planet’s motion is stochastic (e.g., (Hahn & Malhotra 1999)). Because the planet migration rates up to this point in the simulation are not significantly different in the two simulations, we attribute the difference in resonance population to either reduced capture because of a higher initial eccentricity distribution or because of a reduced lifetime in resonance. There are particles present in mean motion resonances in simulation C1 however the fraction of particles captured in resonances is small compared to that in simulation N1 lacking disk self-gravity.

3.2 Effects of disk self-gravity and disk and particle mass on the planet migration rate

In Figure 4 we show the semi-major axis of the outer planet as a function of time for simulations C1 - C10 (with disk self-gravity) and for simulations N1- N10 (lacking disk self-gravity). Since the simulations shown in this figure have planetesimals all of the same mass, the simulations with more particles have higher disk masses. We find that more massive disks allow the outer planet to migrate faster, as might be expected from scaling models predicting migration rates and previous numerical studies (e.g., Hahn & Malhotra 1999; Gomes et al. 2004). In Figure 4 we see that there are jumps in the semi-major axes profiles with time, particularly for the lower mass disks with the slowest migration rates. These correspond to times when the two planets pass through a mean motion resonance. As the planets are separating, the outer planet is not captured into resonance, rather it jumps from one side of the resonance to the other. For a short time the planet eccentricities increase and then are damped via scattering with planetesimals (a form of dynamical friction). The jumps in both eccentricity and semi-major axis, we see in both the self-gravitating

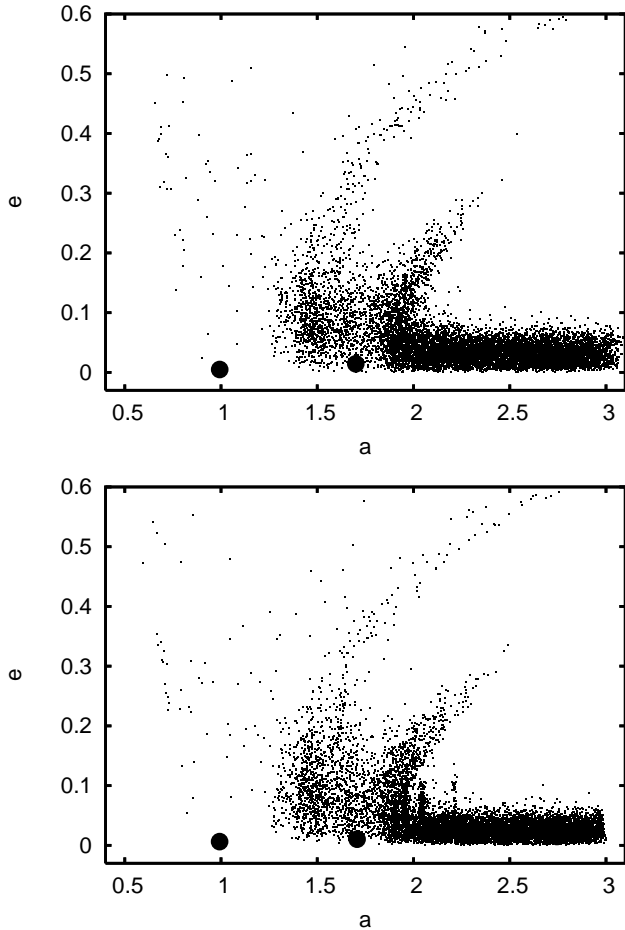


Figure 3. Eccentricity vs semi-major axis distribution at a time $t = 557$ rotation periods. Planets are shown with filled in circles, planetesimals with small dots. Scattering surfaces with periastrons that are planet crossing are seen for both planets. a) For simulation C1 including planetesimal gravitational interactions. b) For simulation N1 lacking planetesimal interactions. In simulation N1 particles have been captured in the 4:3 and 3:2 mean motion resonances at semi-major axes of 2.06 and 2.23 for the planet at a semi-major axis at 1.7. The outer disk in simulation C1 is thicker and lacks as numerous a resonant population as simulation N1. In simulation C1 either planetesimal interactions have scattered planetesimals out of resonances or the fraction of particles captured into resonances is reduced because of the higher eccentricity distribution resulting from gravitational stirring.

and non-self-gravitating simulations and are particularly noticeable when the disk is low mass and the migration rate slow. These resonant events have been previously seen in other numerical simulations, for example such an event is an important characteristic of the “Nice” model for the outward migration of the outer planets in the early solar system (Tsiganis et al. 2005; Levison et al. 2008).

We notice differences in the migration rates in the self-gravitating disk compared to that lacking self-gravity. On average the total distance traveled by the outer planet is higher when self-gravity is absent, as shown in Figure 5 showing the total distance traveled by the outer planet after 4000 orbits. However when we examine the total distance traveled by the outer planet, we note that the self-

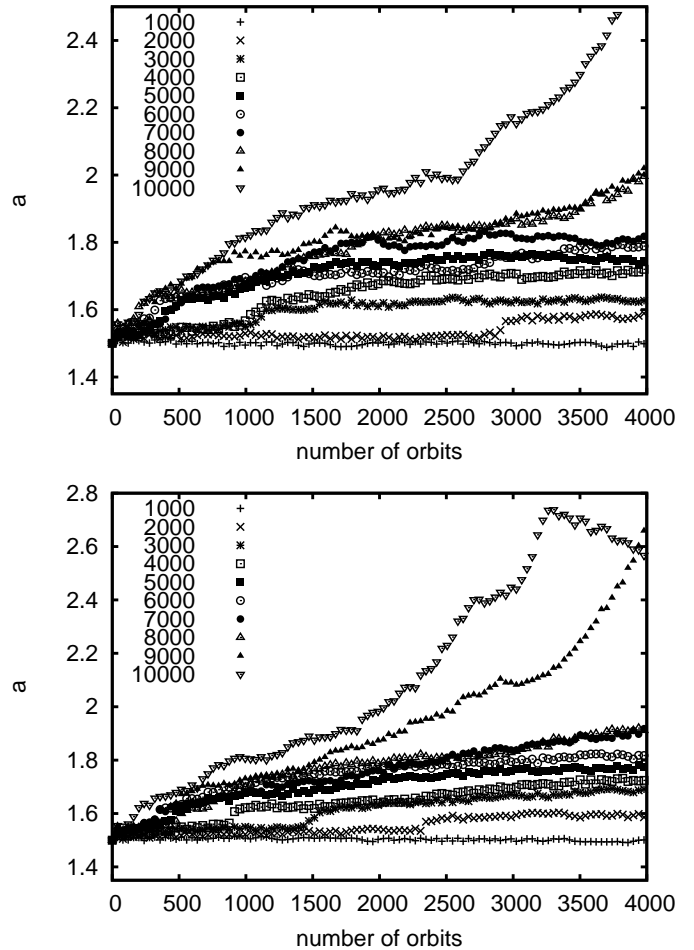


Figure 4. The outer planet’s semi-major axis as a function of time. a) For simulations C1 through C10, computing all pairwise forces. b) For simulations N1 through C10, lacking disk self gravity. Jumps in the semi-major axis occur when the two planets pass through resonance. The migration rate is approximately proportional to the disk density. Stronger migration is seen at the largest disk densities. Migration is not damped but neither is it exponentially increasing in these simulations. This suggests that the migration rate saturates at a level that depends on disk density.

gravitating simulations have much larger scatter in this quantity than those lacking self gravity. The planets in the simulations lacking self-gravity tend to have smoother migration excepting when the disk is very massive.

For the most massive disks considered we note that the migration rate strongly increases with time for both self-gravitating and non-self gravitation simulations (see Figure 4). These may represent migration in the exponential or “forced” regime predicted under some conditions by Gomes et al. (2004).

Following the toy model by Gomes et al. (2004) (see their equations 1-3) the planet migration rate, \dot{a}_p is expected to depend on the total mass of orbit crossing planetesimals $M(t)$

$$\dot{a}_p \approx \frac{k}{2\pi} \frac{M(t)}{M_p} \frac{1}{\sqrt{a_p}}, \quad (10)$$

where k is a possibly migration rate dependent function that depends on the distribution of the planet crossing planetesimal orbits, M_p is the mass of the planet, and a_p is the planet's semi-major axis. The evolution of $M(t)$ depends on the timescale, τ , for the planet to scatter planetesimals away so that they are no longer orbit crossing (also possibly migration rate dependent) and the additional mass in planetesimals that becomes orbit crossing because the planet has moved further into the unscattered disk;

$$\dot{M}(t) = -M(t)/\tau + 2\pi a_p |\dot{a}_p| \sigma(a_p), \quad (11)$$

where $\sigma(a)$ is the surface density of the unscattered planetesimal disk.

The sign of the parameter

$$\alpha = -\tau^{-1} + k\sqrt{a_p}\sigma(a_p)/M_p \quad (12)$$

determines whether the migration is damped or forced. If $\alpha < 0$ then $M(t)$ decays exponentially and the planet stops migrating, otherwise the planet accelerates. For the most massive disks considered here we do see accelerations in the migration rate, and for the lowest density disks we see little migration. However for most of our simulations we see smooth or nearly powerlaw migration rates. For the migration rate to fail to be exponential we require that $\alpha \approx 0$. There could be an intermediate of disk densities, in between the forced and damped regimes, where k and τ can be considered functions of the migration rate. Alternatively the migration could increase until a saturation level which depends on disk density. We note that the disks we consider are more massive than required for migration; $\sigma(r)r^2 \gtrsim M_p$. For the massive disks a larger population of scattered objects is left after the planet passes through the disk implying that only a fraction of it has efficiently imparted energy and angular momentum to the planet. The planet scatters particles at lower efficiency during more rapid migration. This would lower k and τ possibly accounting for the near cancellation of the two terms comprising α .

We now fix the mass of the disk and consider how the mass of the particles affect the migration rates. In the V1-V10 simulations we altered the mass of the planetesimals such that no matter what number of particles there were, the total disk mass was always a Jupiter mass. Figure 6 shows the distance traveled by the outer most planet and semi-major axis as a function of time for 3 simulations. While Figure 6a shows a substantial variation in the total distance traveled by the planets in these simulations but no strong dependence on the planetesimal mass. Figure 6b, showing the semi-major axis profiles shows that the migration of the outer planet is far more stochastic when the planetesimal mass is higher as explored by previous studies (Hahn & Malhotra 1999; Zhou et al. 2002; Murray-Clay & Chiang 2006).

4 SUMMARY AND DISCUSSION

In this paper we have described an implementation of the heliocentric democratic 2nd order symplectic integration scheme (Duncan et al. 1998) written in CUDA and designed to work on a graphics processing unit. This allows us to efficiently use the large number of processors available on the card in parallel. The code is designed to compute a

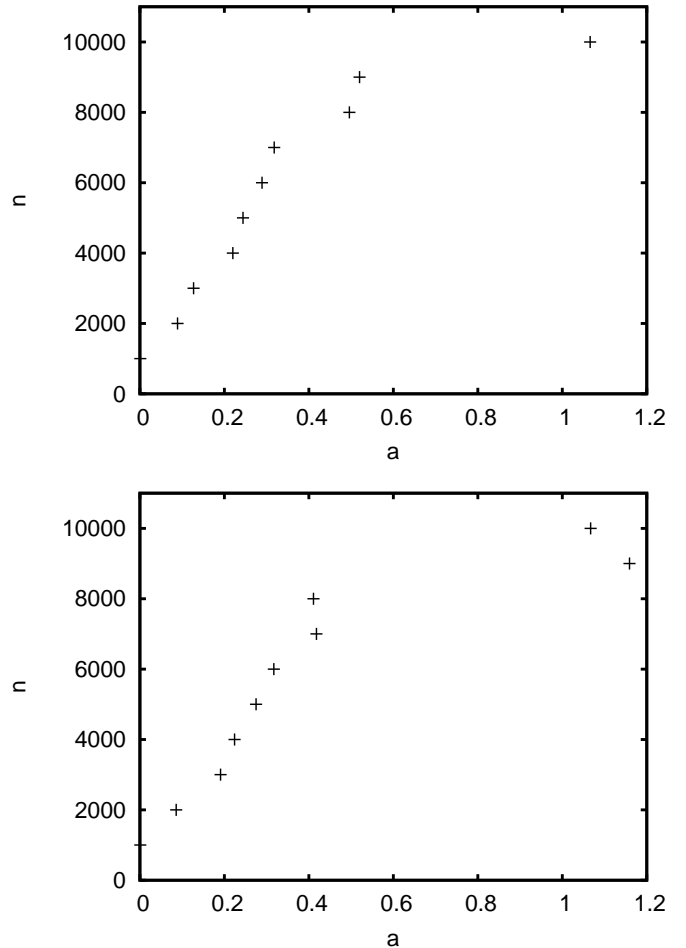


Figure 5. The total distance (x -axis) migrated by the outer planet after 4000 orbits as a function of number of planetesimals in the disk (y -axis). a) As measured from simulations C1-C10 which compute all pair-wise forces. b) As measured from simulations N1-N10 which neglect the self-gravity of the planetesimals. For these simulations the planetesimals have the same mass so the particle number sets the total disk mass. We find that the outermost planet migrates faster in proximity to a more massive planetesimal disk at rate that is approximately proportional to the disk density. The planetary migration rate is on average ~ 1.3 times higher when disk self-gravity is neglected. The lines show the best fit to the data points.

large number of gravitational interactions as well as compute Keplerian advances in parallel. Because all memory resides on the device this parallel computation platform has advantages over message passage interfaces that must pay a penalty to share information between processors. The biggest drawback with our current computational platform is the low precision, a problem that is now being resolved with the recent availability of double precision capable video cards.

We have used the new code to simulate planetary migration into a planetesimal disk with 10^4 bodies and have computed all gravitational interactions. We have explored the difference between simulations of planets migrating into self-gravitating planetesimal disks and those lacking computed interactions between planetesimals. We find that the fraction

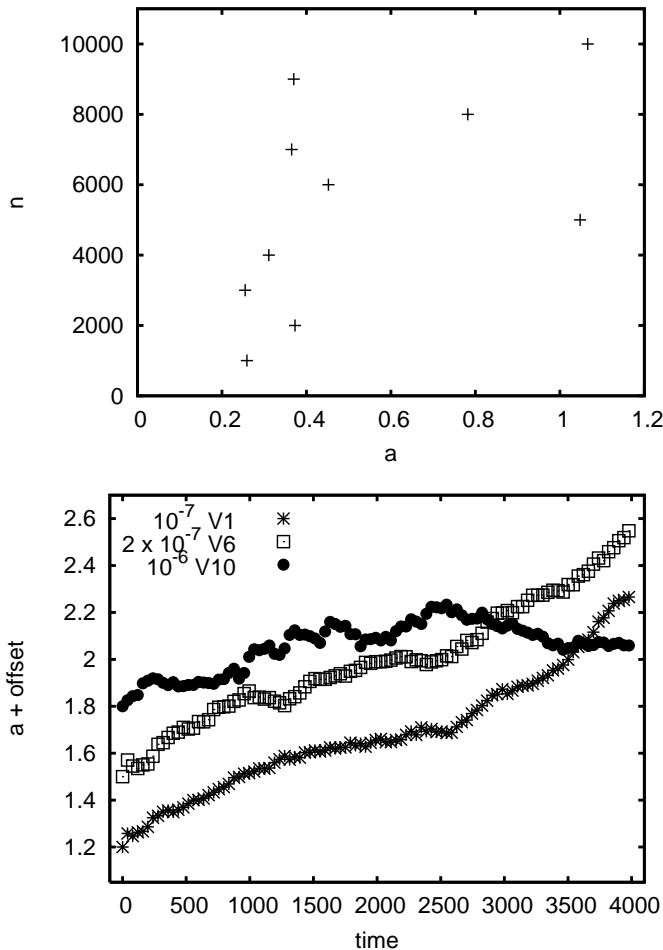


Figure 6. a) The total distance traveled by the outer planet in 4000 orbits as a function of the number of planetesimals in the disk for simulations V1-V10. For these simulations the total disk mass is held fixed so that the planetesimal number is inversely proportional to their mass. The total distance traveled by the outer planet is not strongly dependent on the mass of the planetesimals. b) The semi-major axis as a function of time in orbits for simulations V1, V6, and V10, with the same disk mass but different masses and numbers of planetesimals. The three sets of data points have semi-major axes offset by 0.3 so the three trajectories can be seen together on the same plot. The key lists the simulations and planetesimal mass ratios for those simulations. The planet motion is more stochastic when the planetesimals are more massive.

of particles present in mean motion resonances is reduced in the simulations with self-gravitating disks compared to those lacking planetesimal interactions. We attribute this to a reduction in the resonance capture rate due to the larger eccentricity dispersion caused by gravitational stirring in the self-gravitating planetesimal disks. This suggests that disks in proximity to migrating planets could be featureless (as is true for Fomalhaut, Kalas et al. 2005). A dust disk lacking resonant structure could still host migrating planets.

We find that planet migration is smoother but somewhat faster in the simulations lacking self-gravity. Migration rates in both cases are approximately linearly dependent on planetesimal disk density. The planet can undergo rapid changes in migration in the simulations with the most

massive disks. However for the most of the disk densities considered no exponential increase in migration rate is seen implying that the migration rate saturates at a level approximately proportional to the disk density.

We thank Matt Holman for suggesting how to reduce the radial drift caused by single precision computation during the Keplerian computation step. Support for this work at University of Rochester and Rochester Institute of Technology was also provided by NASA through an award issued by JPL/Caltech, by NSF grants AST-0406823 & PHY-0552695 and HST-AR-10972 to the Space Telescope Science Institute. This work is based on observations made with the Spitzer Space Telescope, which is operated by the Jet Propulsion Laboratory, California Institute of Technology under a contract with NASA.

REFERENCES

- Bromley, B. C., & Kenyon, S. J. 2006, *AJ*, 131, 2737
 Dominik, C., & Decin, G. 2003, *ApJ*, 598, 626
 Duncan, M. J., Levison, H. F., & Lee, M. H. 1998, *AJ*, 116, 2067
 Wisdom, J., Holman, M., & Touma, J. 1996, *Fields Institute Communications*, 10, 217
 Fernandez, J. A., & Ip, W.-H. 1984, *Icarus*, 58, 109
 Gomes, R. S., Morbidelli, A., & Levison, H. F. 2004, *Icarus*, 170, 492
 Gomes, R., Levison, H. F., Tsiganis, K., & Morbidelli, A. 2005, *Nature*, 435, 466
 Hahn, J. M., Malhotra, R. 2005, *AJ*, 130, 2392
 Hahn, J. M., & Malhotra, R. 1999, *AJ*, 117, 3041
 Harris, M., Sengupta, S., & Owens, J. D. 2008, Chap 39 in *GPUGems3*, edited by Hubert Nguyen, 2008, Addison-Wesley, Upper Saddle River, NJ, page 851
 Kalas, P., Graham, J. R., & Clampin, M. 2005, *Nature*, 435, 1067
 Ida, S., Bryden, G., Lin, D. N. C., & Tanaka, H. 2000, *ApJ*, 534, 428
 Kokubo, E., & Ida, S. 1995, *Icarus*, 114, 247
 Levison, H. F., Morbidelli, A. 2003, *Nature*, 426, 419
 Levison, H. F., Morbidelli, A., Vanlaerhoven, C., Gomes, R., & Tsiganis, K. 2008, *Icarus*, 196, 258
 Lufkin, G., Richardson, D. C., & Mundy, L. G. 2006, *ApJ*, 653, 1464
 Malhotra, R. 1995, *AJ*, 110, 420
 Morbidelli, A. 2001, *Ann. Rev. Earth and Pl. Sci.*, 30, 89
 Murray-Clay, R. A., & Chiang, E. I. 2006, *ApJ*, 651, 1194
 Nyland, L., Harris, M., & Prins, J. 2008, Chap 31 in *GPUGems3*, edited by Hubert Nguyen, 2008, Addison-Wesley, Upper Saddle River, NJ, page 677
 Prussing, J. E. & Conway, B. A. 1993, *Orbital Mechanics*, Oxford University Press, Inc., New York, New York
 Quillen, A. C., Morbidelli, A., & Moore, A. 2007, *MNRAS*, 380, 1642

- Quillen, A. C. 2006, MNRAS, 372, L14
Quillen, A. C. 2006, MNRAS, 365, 1367
Thommes, E. W., Bryden, G., Wu, Y., & Rasio, F. A. 2008, ApJ, 675, 1538
Tsiganis, K., Gomes, R., Morbidelli, A., & Levison, H. F. 2005, Nature, 435, 459
Wyatt, M. C., & Dent, W. R. F. 2002, MNRAS, 334, 589
Wyatt, M. C 2006, ApJ, 639, 1153
Yoshida, H. 1990, Phys. Lett. A, 150, 262
Zhou, L.-Y., Sun, Y.-S. Zhou, J.-L., Zheng, J.Q., & Valtonen, M. 2002, MNRAS, 336, 520

Table 1. Simulations

Simulation	M_1	a_1	M_2	a_2	m	N	M_d
C1	10^{-3}	1.0	5×10^{-5}	1.5	10^{-7}	10^4	10^{-3}
C2	10^{-3}	1.0	5×10^{-5}	1.5	10^{-7}	9×10^3	9×10^{-4}
C3	10^{-3}	1.0	5×10^{-5}	1.5	10^{-7}	8×10^3	8×10^{-4}
C4	10^{-3}	1.0	5×10^{-5}	1.5	10^{-7}	7×10^3	7×10^{-4}
C5	10^{-3}	1.0	5×10^{-5}	1.5	10^{-7}	6×10^3	6×10^{-4}
C6	10^{-3}	1.0	5×10^{-5}	1.5	10^{-7}	5×10^3	5×10^{-4}
C7	10^{-3}	1.0	5×10^{-5}	1.5	10^{-7}	4×10^3	4×10^{-4}
C8	10^{-3}	1.0	5×10^{-5}	1.5	10^{-7}	3×10^3	3×10^{-4}
C9	10^{-3}	1.0	5×10^{-5}	1.5	10^{-7}	2×10^3	2×10^{-4}
C10	10^{-3}	1.0	5×10^{-5}	1.5	10^{-7}	10^3	10^{-4}
N1	10^{-3}	1.0	5×10^{-5}	1.5	10^{-7}	10^4	10^{-3}
N2	10^{-3}	1.0	5×10^{-5}	1.5	10^{-7}	9×10^3	9×10^{-4}
N3	10^{-3}	1.0	5×10^{-5}	1.5	10^{-7}	8×10^3	8×10^{-4}
N4	10^{-3}	1.0	5×10^{-5}	1.5	10^{-7}	7×10^3	7×10^{-4}
N5	10^{-3}	1.0	5×10^{-5}	1.5	10^{-7}	6×10^3	6×10^{-4}
N6	10^{-3}	1.0	5×10^{-5}	1.5	10^{-7}	5×10^3	5×10^{-4}
N7	10^{-3}	1.0	5×10^{-5}	1.5	10^{-7}	4×10^3	4×10^{-4}
N8	10^{-3}	1.0	5×10^{-5}	1.5	10^{-7}	3×10^3	3×10^{-4}
N9	10^{-3}	1.0	5×10^{-5}	1.5	10^{-7}	2×10^3	2×10^{-4}
N10	10^{-3}	1.0	5×10^{-5}	1.5	10^{-7}	10^3	10^{-4}
V1	10^{-3}	1.0	5×10^{-5}	1.5	10^{-7}	10^4	10^{-3}
V2	10^{-3}	1.0	5×10^{-5}	1.5	1.085×10^{-7}	9×10^3	10^{-3}
V3	10^{-3}	1.0	5×10^{-5}	1.5	1.25×10^{-7}	8×10^3	10^{-3}
V4	10^{-3}	1.0	5×10^{-5}	1.5	1.4×10^{-7}	7×10^3	10^{-3}
V5	10^{-3}	1.0	5×10^{-5}	1.5	1.67×10^{-7}	6×10^3	10^{-3}
V6	10^{-3}	1.0	5×10^{-5}	1.5	2.0×10^{-7}	5×10^3	10^{-3}
V7	10^{-3}	1.0	5×10^{-5}	1.5	2.5×10^{-7}	4×10^3	10^{-3}
V8	10^{-3}	1.0	5×10^{-5}	1.5	3.25×10^{-7}	3×10^3	10^{-3}
V9	10^{-3}	1.0	5×10^{-5}	1.5	5×10^{-7}	2×10^3	10^{-3}
V10	10^{-3}	1.0	5×10^{-5}	1.5	10^{-6}	10^3	10^{-3}

Here M_1 , M_2 are the masses of the two planets, and m is the planetesimal mass in units of the central star mass. The parameters a_1 and a_2 are the initial planet semi-major axes. The parameter N is the total number of planetesimals, and M_d is the total planetesimal disk mass in units of the stellar mass. The planetesimals initially extend between 1.5 and 3.0 in semi-major axis. Simulations C1-C10 included all pair-wise forces all have the same planetesimal masses but a range of total disk masses. Simulations N1-N10 are identical to the C series but neglect interactions between the planetesimals. Simulations V1-V10 compute all pair-wise forces and vary planetesimal mass in order to maintain constant mass disk with a fixed number of particles. Simulations were run for approximately 4000 orbits.